Physics of the Earth and Planetary Interiors 189 (2011) 27–33

Contents lists available at SciVerse ScienceDirect

Physics of the Earth and Planetary Interiors

journal homepage: www.elsevier.com/locate/pepi

Control of the water fugacity at high pressures and temperatures: Applications to the incorporation mechanisms of water in olivine

Kazuhiko Otsuka *, Shun-ichiro Karato

Department of Geology and Geophysics, Yale University, New Haven, CT 06511, USA

ARTICLE INFO

Article history:
Received 13 July 2011
Received in revised form 13 September 2011
Accepted 16 September 2011
Available online 24 September 2011
Edited by Kei Hirose

Keywords:
Water fugacity
Olivine
Point defects
Infrared spectroscopy

ABSTRACT

A new method is developed to control water fugacity at a fixed pressure and temperature. We use two divariant phase assemblages (clinohumite–periclase–forsterite and brucite–periclase) in the MgO–SiO_2–H_2O system and the chemical reactions among co-existing phases buffer the water fugacity. In order to avoid a reaction between the water fugacity buffer and the specimen, a double-capsule assemblage was designed such that the water fugacity buffer was separated from the specimen by an inner metal jacket permeable to hydrogen and impermeable to other components. This method was applied to investigate the incorporation mechanisms of water in single crystals of San Carlos olivine as a function of water fugacity at 5 GPa and 1273 K. The chemical environment of the olivine crystal was controlled by the water fugacity buffer, the Ni–NiO oxygen fugacity buffer, and the olivine–orthopyroxene silica activity buffer. The establishment of chemical equilibrium was demonstrated by the presence of all relevant phases in the buffering reactions. The effect of water fugacity on water concentration in olivine was investigated using Fourier transform infrared (FTIR) spectroscopy with a polarized light. The total water concentration is nearly linearly dependent on water fugacity, indicating that the dominant incorporation mechanism of water in olivine involves two hydrogen atoms substituted in a Mg-site vacancy. The proposed method of the water fugacity buffer can be applicable to investigate the role of water in various important properties including water solubility and partitioning between mantle minerals, rheological properties, electrical conductivity, as well as solidus temperatures.

1. Introduction

The water fugacity, f_{H_2O} (or the chemical potential of water) is a key factor to control several important physical and chemical properties of materials in the Earth's mantle. Small amounts of water dissolved in nominally anhydrous minerals including olivine significantly enhance atomic diffusivity (e.g., Costa and Chakraborty, 2008; Hier-Majumder et al., 2005) plastic deformation (e.g., Hirth and Kohlstedt, 2003; Karato and Jung, 2003; Mei and Kohlstedt, 2000), and electrical conductivity (e.g., Wang et al., 2006; Yoshino et al., 2009). In addition, the presence of water drastically changes the melting temperature, liquidus phases and the coexisting melt composition in the mantle peridotite system (e.g., Inoue, 1994; Kawamoto, 2004). To understand the microscopic mechanisms of water-sensitive properties, it is important to place these results in a thermodynamic framework including f_{H_2O}. It will also allow us to compare separate experimental results to one another.

However, in the previous laboratory studies in a solid-medium high-pressure apparatus f_{H_2O} was not controlled as an independent variable. Instead, experiments were conducted either under water-saturated conditions with an excess fluid phase (e.g., Hier-Majumder et al., 2005; Kohlstedt et al., 1996), or under fluid-absent conditions with the specimen containing a specific water concentration (e.g., Wang et al., 2006; Yoshino et al., 2009). In the former case, the range of f_{H_2O} is generally explored as a dependent variable by changing the confining pressure. Pressure generally affects properties not only through the pressure dependence on f_{H_2O} but also through the term involving pressure and activation volume of the property of interest (or the volume change associated with the process of interest). If one explores a narrow pressure interval at high pressures, the separation of the f_{H_2O} effect from that of the intrinsic pressure-volume term is difficult because of the similarity in the functional form between the two terms. Alternatively, if one explores a wide pressure range, the fugacity exponent can be constrained better. The underlying assumption is that the fugacity exponent stays constant over the pressure range (i.e., the mechanism of the water-sensitive property does not change with pressure). However, the validity of this assumption is questionable because several different hydrogen-related defect species co-exist in a given material (e.g., Keppler and Bolfan-Casanova, 2006) and the relative importance for water-related properties likely changes with pressure, temperature and water concentration. As a result, previous studies are subject to uncertainties in inferring the

* Corresponding author.
E-mail address: kazuhiko.otsuka@yale.edu (K. Otsuka).

0031-9201/$ - see front matter © 2011 Elsevier B.V. All rights reserved.
doi:10.1016/j.pepi.2011.09.007

microscopic mechanisms of water-related properties (for more detailed discussion, see Appendix). Another limitation is the fact that a thermodynamic model is required to extrapolate data from water-saturated conditions to more appropriate lower water concentrations. In the latter case (water-undersaturated conditions), the influence of f_{H_2O} cannot be determined without combining a thermodynamic model of the dependence of f_{H_2O} on water solubility. Furthermore, because f_{H_2O} is not explicitly controlled during experiments, water loss or gain causes uncertainties in quantifying the influence of water contents.

Consequently, it is critical to develop a method to control f_{H_2O} as an independent variable at a fixed pressure and temperature condition. This paper describes a new method to control f_{H_2O} at high-pressure and high-temperature conditions.

2. Methods

We use solid-state divariant phase assemblages to control f_{H_2O}. This method is similar to the metal-oxide oxygen fugacity buffer commonly used in a multi-anvil apparatus (e.g., Otsuka et al., 2010). The f_{H_2O} corresponding to each buffer can be calculated as follows. Consider a chemical system containing hydrous phase $Z(H_2O)_x$ and anhydrous phase Z under water-undersaturated conditions (i.e., under water-absent conditions). A chemical reaction involving H_2O as an exchange component in compositional space (see Thompson, 1982) has the form:

$$Z(H_2O)_x = Z + xH_2O \quad (1)$$

Note that H_2O does not exist as a separate phase. At the equilibrium, the chemical potential of water in the system is expressed as:

$$\mu_{H_2O} = \frac{1}{x}(\mu_{Z(H_2O)_x} - \mu_Z) \quad (2)$$

where μ is the chemical potential of the phase denoted by the subscript at pressure and temperature of interest (P and T). Taking a reference state at pressure P_0 and temperature T, f_{H_2O} in the system is related to the chemical potential of corresponding phases in the system:

$$\mu_{H_2O}(P,T) = \mu^0_{H_2O}(P_0,T) + RT\ln\frac{f_{H_2O}}{P_0} \quad (3)$$

where μ^0 is the chemical potential at the reference state, R is the gas constant. Note that any divariant assemblage containing a H_2O component constrains f_{H_2O} at a given pressure and temperature condition independent of concentration of each phase.

In this study, f_{H_2O} of the system was buffered by assemblages in the MgO–SiO_2–H_2O (MSH) system. Fig. 1 shows the ternary phase diagram for the MSH system at the experimental condition (5 GPa and 1273 K) based on Wunder (1998). The phase diagram indicates three divariant mineral assemblages at water-undersaturated conditions as potential candidates for f_{H_2O} buffers: clinohumite–periclase–forsterite (CH–Per–Fo buffer), chondrodite–clinohumite–periclase (Cd–CH–Per buffer), and brucite–periclase (Br–Per buffer) in the order of increasing f_{H_2O}. Among the three buffers, this study used CH–Per–Fo and Br–Per buffers. Fig. 1 also plots estimated composition of fluid coexisting with olivine and orthopyroxene based on Mibe et al. (2002) at 5 GPa and 1373 K, which is above the second critical point at 3.8 GPa and 1273 K for the peridotite–H_2O system where aqueous fluid and silicate melt becomes indistinguishable (Mibe et al., 2007).

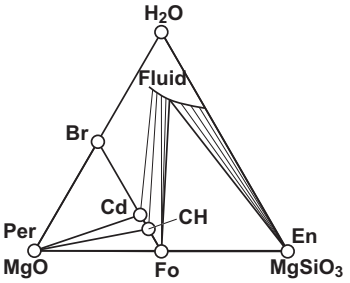

Fig. 1. Ternary phase diagram for the MgO–SiO_2– H_2O (MSH) system in the molar ratio at 5 GPa and 1273 K. Br: $Mg(OH)_2$ brucite, Cd: $Mg_5Si_2O_8(OH)_2$ chondrodite, CH: $Mg_9Si_4O_{16}(OH)_2$ clino-humite, En: $MgSiO_3$ enstatite, Fluid: supercritical fluid, Fo: Mg_2SiO_4 forsterite, Per: MgO periclase. Composition of fluid was estimated from Mibe et al. (2002) at 5 GPa and 1373 K.

Fig. 2 shows a complied phase diagram in the water fugacity assemblages in the MSH system based mostly on Wunder (1998). The P–T stability condition of the Br–Per buffer is defined by that of brucite, for periclase is always stable within the stability field of brucite. At low pressures brucite dehydrates to produce periclase and fluid (Johnson and Walker, 1993). At P > 11 GPa brucites melts incongruently and solidus temperature of brucite decreases with pressure from 1200 °C at 11 GPa to ~1000 °C at 15 GPa (Fukui et al., 2005). The assemblage CH–Per–Fo is stable from 2 GPa and 900 °C up to 11 GPa ~1200 °C, and above that pressure clinohumite decompose through the reaction CH = Cd + Fo (Yamamoto and Akimoto, 1977; Wunder, 1998). The assemblage Cd–CH–Per is stable from 3 GPa and 1000 °C up to the high-P stability limit for clinohumite (Yamamoto and Akimoto, 1977; Wunder, 1998). To our knowledge, high-P stability limit for chondrodite is not well known. The temperature of wet melting in the Fo–En–H_2O system, indicated as a drastic increase in the amount of silicate rich quench products, decreases from ~1325 °C at 2.5 GPa to ~1175 °C at 9 GPa (Bali et al., 2008). Like the Fo–En–H_2O system, the high-P, T stability field of the CH–Per–Fo and Cd–CH–Per assemblages may be affected by the change in silicate solubility in fluid in the Per–Fo–H_2O system.

The f_{H_2O} buffers mentioned above do not coexist with the peridotite (olivine and orthopyroxene) assemblage (Fig. 1). Thus, in order to avoid chemical reaction with the specimen, a double-capsule assemblage illustrated in Fig. 3 was designed after Edgar (1973). The key point of this modified double-capsule assemblage is that the f_{H_2O} buffer was separated from the specimen by the inner metal jacket permeable to hydrogen and impermeable to other components during experimental durations. The outer Pt capsule contains a mixture of a f_{H_2O} buffer and the inner Ni capsule contains the specimen olivine + orthopyroxene and NiO to oxidize

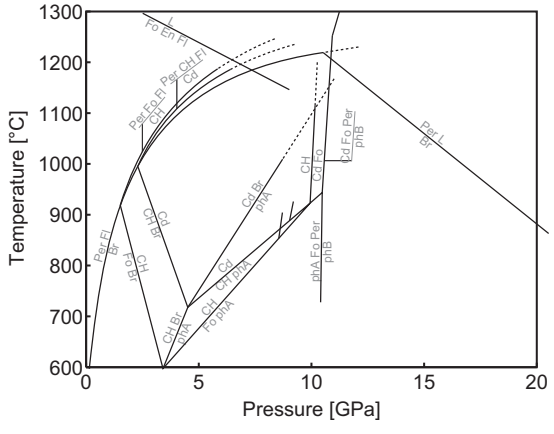

Fig. 2. Phase diagram in the system MgO–SiO_2–H_2O, especially focuses on the Br–Per, Cd–CH–Per and CH–Per–Fo assemblages. Br: $Mg(OH)_2$ brucite, Cd: $Mg_5Si_2O_8(OH)_2$ chondrodite, CH: $Mg_9Si_4O_{16}(OH)_2$ clino-humite, En: $MgSiO_3$ enstatite, Fl: aqueous-rich supercritical fluid, Fo: Mg_2SiO_4 forsterite, L: silicate-rich supercritical fluid, Per: MgO periclase, phA: $Mg_7Si_2O_8(OH)_6$ phase A, phB: $Mg_{24}Si_8O_{38}(OH)_4$ phase B.

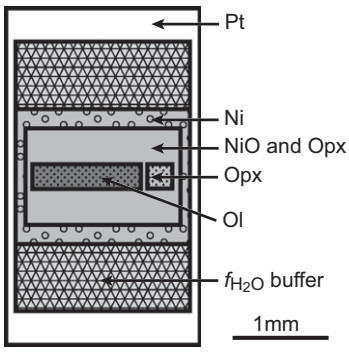

Fig. 3. Schematic diagram of capsule assembly.

hydrogen while maintaining oxygen fugacity as described below. At high *P*–*T* condition, the chemical environment of the specimen approaches towards the one controlled by the buffers, presumably in the following way. First, a reaction between the H_2O component in the f_{H_2O} buffer and the Ni inner capsule produces H in conjunction with NiO:

$$Ni + \underset{\text{buffer}}{\underline{H_2O}} = NiO + H_2 \quad (4)$$

Second, H atoms, or dissociated protons, diffuse into the sample charge through the inner Ni capsule, and reacts with NiO in the sample chamber to form H_2O components:

$$NiO + H_2 = Ni + \underset{\text{sample}}{\underline{H_2O}} \quad (5)$$

It subsequently reacts with orthopyroxene to form hydrous olivine:

$$H_2O + \underset{\text{orthopyroxene}}{\underline{MgSiO_3}} = \underset{\text{olivine}}{\underline{(Mg,H)_2SiO_4}} \quad (6)$$

where Mg-sites in olivine are partly occupied by H. The flow of H, or protons, continues until μ_{H_2O} in reaction (4) equilibrates with that of f_{H_2O} buffer in reaction (5) unless Ni or NiO is completely consumed. In other words, f_{H_2O} in the sample charge builds up until it reaches that of the f_{H_2O} buffer. Thus, the chemical environment of the specimen during annealing is controlled by f_{H_2O} and f_{O_2} buffers.

3. Experimental and analytical procedures

3.1. Experimental procedures

We used single crystals of San Carlos olivine ($(Mg_{0.90}Fe_{0.10})_2SiO_4$) as a sensor of the f_{H_2O} buffer. The olivine single crystal has the initial water content close to 1 ppm H_2O by weight. The crystal was orientated by electron-backscattered diffraction (EBSD) such that the surfaces of the rectangular prism were perpendicular to the three principal axes. The oriented olivine crystal was enclosed in a Ni foil capsule together with orthopyroxene single crystals and a mixture of 50 wt% of NiO and 50 wt% of orthopyroxene. The inner capsule holding the sample charge was crimped closed to seal. This foil capsule was in turn placed in a Pt tube capsule together with a mixture of CH–Per–Fo or Br–Per f_{H_2O} buffer. The starting materials for the f_{H_2O} buffers were mixtures of SiO_2, MgO, and $Mg(OH)_2$ powders in the following compositions: $CH_{90}Fo_5Per_5$ and Br_{100} in weight ratio for CH–Per–Fo and Br–Per buffers, respectively. The Pt capsule was welded to minimize the water input and loss from the surrounding environment.

High-pressure and high-temperature annealing experiments were conducted in a 1000-ton Kawai-type multi-anvil apparatus installed at Yale University. Cell assemblies and experimental protocol are similar to those used by Otsuka et al. (2010). Eight tungsten carbide cubes with an edge length of 26 mm and a corner truncation of 11 mm compress samples contained in a spinel-doped MgO octahedron with an edge length of 18 mm. The sample was pressurized to a specific target load at room temperature, subsequently heated by applying a current across a stepped graphite furnace and then quenched to room temperature by cutting the power to the furnace. Temperature was monitored with a $W_{95}Re_5$–$W_{74}Re_{26}$ thermocouple without pressure correction. The recovered charges from annealing experiments were mounted in epoxy resin and sectioned perpendicular as well as parallel to the cylindrical axis of the sample capsule. Subsequently, the charges were first singly-polished for textural analysis and then doubly-polished to a thickness of 50–200 μm for measurements of water concentration.

3.2. Analytical procedures

Textural analysis and phase identification of the sample charges were conducted using a field-emission-gun scanning electron microprobe (XL30 ESEM-FEG) attached with the energy dispersive X-ray spectroscopy (SEM-EDS) complemented by Raman spectroscopy.

IR absorption spectra of the recovered olivine single crystals were obtained by Fourier transform infrared spectroscopy (FTIR). A Digilab Excalibur 3000 was used with a KBr beam splitter and a mercury cadmium telluride (MCT) detector attached to UMA-600 FTIR microscope. Polarized IR absorption spectra were recorded by more than 512 scans, in some cases up to 2048 scans, at a wavenumber resolution of 1 or 2 cm^{-1}, with the electric field vector, *E*, parallel to the three crystallographic directions of olivine: [100] (*E*//*a*), [010] (*E*//*b*), and [001] (*E*//*c*). The microscope was purged with dry air to minimize the water contamination from the ambient atmosphere. Background in the spectra was removed using a linear fit of the baseline defined by two points outside the hydroxyls (OH) stretching vibrations at approximately 3000 and 4000 cm^{-1}. In some spectra with obvious fringes, the spline interpolation is applied to smoothly define the baseline.

To determine the concentrations of dissolved water in specimens, polarized IR spectra with *E* parallel to the three principal axes were individually integrated over the wavenumber from 3100 to 3700 cm^{-1}. The total water concentrations were calculated by summing the water concentrations with *E* parallel to three principal axes. We used the calibration of Bell et al. (2003):

$$C(H_2O) = B_B \int H(\nu) d\nu \quad (7)$$

where $C(H_2O)$ is H_2O concentration in ppm wt H_2O, and $H(\nu)$ is the absorption coefficient in cm^{-1} at wavenumber ν in cm^{-1}. The value of $B_B = 0.188$ [ppm wt H_2O/cm^2] was used (Bell et al., 2003). For the sake of comparison to previous results, we also applied the calibration of Paterson (1982):

$$C(H_2O) = \frac{B_p}{150\zeta} \int \frac{H(\nu)}{3780 - \nu} d\nu \quad (8)$$

where ζ is an orientation factor set to be 1 for the unpolarized radiation. The value of $B_p = 2.81 \times 10^3$ [ppm wt H_2O/cm^2] was used (Kohlstedt et al., 1996). The conversion from $C(H_2O)$ in $H/10^6Si$ to ppm wt H_2O can be approximated as: $C(H_2O)$ [$H/10^6Si$] = 15.62 × $C(H_2O)$ [ppm wt H_2O] for forsterite.

Thermodynamic database we used to calculate f_{H_2O} are from Komabayashi and Omori (2006) and Komabayashi et al. (2005). The H_2O activity was set to be unity assuming low concentration of dissolved Mg and Si components in the fluid. This assumption is probably valid based on temperature dependence of water solubility in olivine determined by previous studies (Bali et al., 2008; Litasov et al., 2007).

Table 1
Experimental results annealed at 5 GPa and 1273 K.

Run	Time (h)	Buffer	fH_2O (GPa)	COH [H_2O wt ppm]			
				E//a B*/P**	*E//b* B*/P**	*E//c* B*/P**	Total B*/P**
Water saturated conditions							
K876	27	–	1.04×10^3	1289/605	796/326	590/250	2676/1181
Water fugacity buffer							
K982	32	Br–Per	4.96×10^2	606/270	274/102	239/93	1120/464
K983	76	Br–Per	4.96×10^2	584/235	251/85	256/89	1091/408
K904	30	CH–Fo–Per	3.55×10^2	536/228	195/76	192/72	924/376
K986	31.1	CH–Fo–Per	3.55×10^2	504/219	173/68	187/74	864/360

Note: B*: calibration by Bell et al. (2003); P*: calibration by Paterson (1982).

4. Results

4.1. Experimental conditions

We performed experiments at a constant pressure and temperature of 5 GPa and 1273 K to anneal olivine single crystals under f_{H_2O} controlled by Br–Per and CH–Per–Fo buffers as well as under water-saturated conditions with fluid for comparison (Table 1). The recovered samples from the annealing experiments with f_{H_2O} controlled by solid-state buffers contain following phases: olivine, orthopyroxene, Ni and NiO in the sample chamber (inner capsule) and the f_{H_2O} buffers in between the inner and outer capsules. Based on the observed mineral assemblage, we infer that the chemical environment in the system was controlled by the following buffers: the f_{H_2O} buffer controlled by either CH–Per–Fo or Br–Per, the olivine–orthopyroxene a_{SiO_2} buffer and the Ni–NiO f_{O_2} buffer. The attainment of chemical equilibrium in terms of the f_{H_2O} is further confirmed by water concentration in olivine with different annealing durations.

4.2. Microstructure

Fig. 4 illustrates the representative textures of the experimental charges with f_{H_2O} controlled by the solid-state f_{H_2O} buffer. The olivine crystal is surrounded by grains of orthopyroxene, NiO and Ni (Fig. 4A) and the original shape of olivine crystals is preserved without any extensive fractures. Olivine is slightly enriched in Ni and depleted in Fe relative to the starting materials. Ni grains with a grain size up to a few tens μm were presumably nucleated and grew from NiO grains with a grain size of a few μm originally added to the sample chamber. The presence of Ni grains indicates that H diffused into the sample chamber and induced the chemical reactions (5) and (6). At the interface of the inner Ni capsule and f_{H_2O} buffer, a polycrystalline NiO layer containing a small amount of Ni grains was formed with the thickness on the order of 100 μm (Fig. 4C). This indicates that the reaction (4) occurred to produce H. The presence of the f_{H_2O} buffers, either Br–Per or CH–Per–Fo, in between the inner Ni and the outer Pt capsules, was confirmed by Raman spectroscopy and electron probe microanalysis.

However, in some runs the breakdown of the Ni membrane occurred that resulted in direct reactions between the f_{H_2O} buffer and the sample charge. These failed experiments were discarded without further investigation of water concentration.

In addition to these experiments, we further tested Mo and Pd inner capsules, containing either MoO_2 or PdO together with the sample charge, as the semi-permeable membrane instead of Ni capsules. Although we conducted experiments at the similar conditions with the Ni–NiO system, the recovered samples did not contain appreciable amounts of Mo or Pd oxide layer at the interface between the inner capsules and f_{H_2O} buffers, nor the Mo or Pd metal in the sample chamber. In these cases, we have no clear evidence for the control of f_{O_2} (and hence f_{H_2O}) by the buffers used. Consequently, results from these runs are not used in this paper. We suspect that the reaction kinetics to produce MoO_2 or PdO is very sluggish compared with NiO.

4.3. Infrared spectra

Fig. 5 shows polarized infrared absorption spectra in the OH stretching region (from 3100 to 3700 cm^{-1}) obtained from the olivine single crystals annealed at 5 GPa and 1273 K with three different f_{H_2O} conditions: water-saturated conditions with super-critical fluid, and f_{H_2O} controlled by Br–Per, and CH–Per–Fo buffers. The general features in the OH stretching bands reported in this study for olivine annealed under water-saturated conditions are consistent with previous studies at similar conditions (Bali et al., 2008; Kohlstedt et al., 1996; Mosenfelder et al., 2006). The IR beam is strongly absorbed within the wavenumber range from 3650 to 3450 cm^{-1} and no significant peaks were found between 3400 and 3100 cm^{-1}. The absorption bands with *E* parallel to *a* axis (*E*//*a*) are strongest within the three principal axes, and found approximately at 3612, 3605, 3578, 3543, and 3477 cm^{-1}. Bands with *E* parallel to *b* axis (*E*//*b*) are located mainly near 3550 cm^{-1} with minor peaks around 3612, 3579, and 3478 cm^{-1}. Bands with *E* parallel to *c* axis (*E*//*c*) are sharp at 3565 cm^{-1} with minor peaks near 3657, 3605, and 3532 cm^{-1}.

4.4. Water concentrations and incorporation mechanisms of water in olivine

Table 1 listed the water concentrations in olivine single crystals obtained from infrared spectra with *E* parallel to the three principal

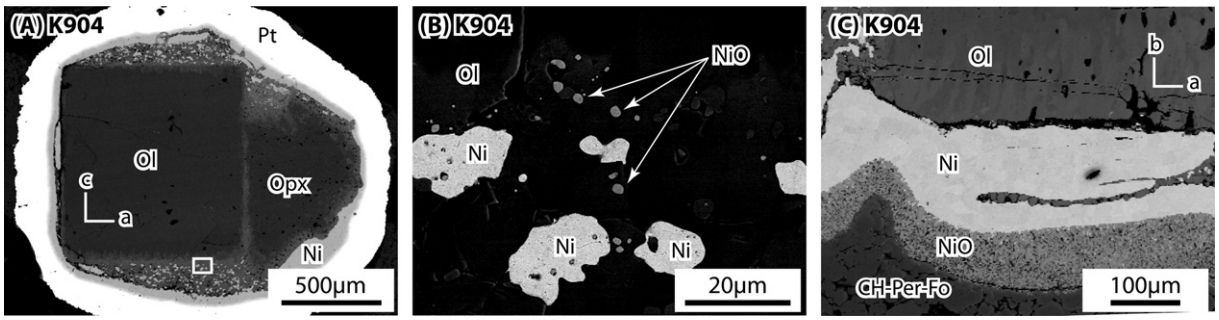

Fig. 4. Back-scattered electron images of K904, annealed with CH–Per–Fo buffer. View from the cylindrical (vertical) axis of sample capsule (A, B) and from the radial (horizontal) direction (C), where the olivine crystal is orientated normal to [010] and [001] direction, respectively. Panel (B) is expansion of the rectangular area in (A).

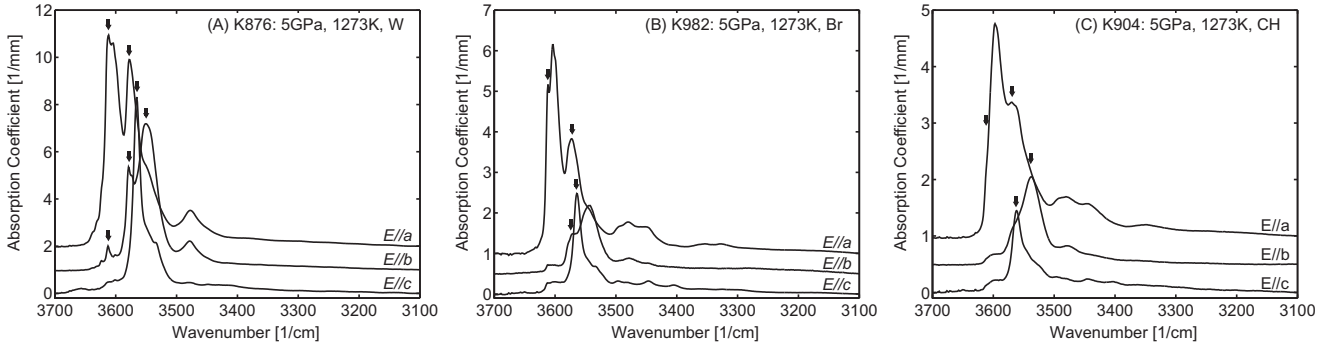

Fig. 5. Polarized FTIR spectra of hydrous olivine annealed at 5 GPa, 1,273 K with different water fugacity buffers: water-saturated (A), Br–Per buffer (B), CH–Per–Fo buffer (C). OH absorption bands sensitive to water fugacity are indicated by arrows.

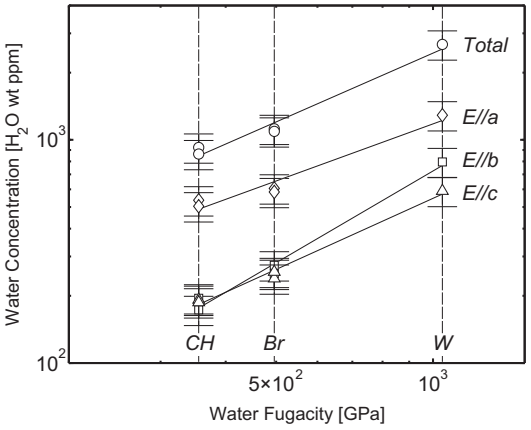

Fig. 6. Water concentration along *a* axis (*E*//*a*), *b* axis (*E*//*b*), *c* axis (*E*//*c*), and the sum of the three axes (total) plotted against water fugacity. W: water saturated conditions, Br: Br–Per buffer, CH: CH–Per–Fo buffer.

crystallographic axes and also total water concentrations by summing the amounts in three axes. A generally consistent result between two experiments with f_{H_2O} buffered by the Br–Per join with different annealing durations (32 and 76 h) indicates that estimated water concentrations were equilibrium values controlled by the f_{H_2O} buffers.

Fig. 6 plots the water concentrations of samples based on the Bell et al. (2003)'s calibration against f_{H_2O} in a log–log plot. We fitted the total water concentration to the equation $C(H_2O) \propto f_{H_2O}^n$ to determine the fugacity exponent, n. The values of n we obtained are 1.0(1) and 1.1(2) for the calibration of Bell et al. (2003) and Paterson (1982), respectively. The almost linear dependence of water solubility on f_{H_2O} indicates that the dominant incorporation mechanism of water in olivine is two protons substituted into a Mg-site vacancy at the condition we explored. This is in reasonable agreement with $n \sim 0.8$ at lower pressures between 50 and 300 MPa obtained by Bai and Kohlstedt (1993) in their experiments using a gas-medium apparatus. The relatively small effect of pressure on n suggests that the dominant incorporation mechanism does not change with pressure in this pressure range.

There is some hint for the presence of hydrogen-related point defects other than two protons at a Mg site suggested by systematic variation of the intensities and frequencies of OH stretching bands with f_{H_2O}. The bands near 3612 cm^{-1} with *E*//*a*, 3612, 3550 cm^{-1} with *E*//*b*, and 3565 cm^{-1} with *E*//*c* become less prominent than others at low f_{H_2O} (more sensitive to f_{H_2O}), while the band near 3605 cm^{-1} with *E*//*a* becomes more prominent (less sensitive to f_{H_2O}) (see Fig. 5). The details about the f_{H_2O} dependence of IR spectra and its implications for hydrogen-related defects will be published elsewhere.

5. Concluding remarks

This study presents a new method to buffer f_{H_2O} by divariant phase assemblages under fluid-absent conditions encapsulated in the modified double-capsule assemblage. This method was applied to investigate incorporation mechanisms of water in olivine as a function of water fugacity at constant pressure 5 GPa and temperature 1273 K, using polarized FTIR spectroscopy. One of the key parameters we explored was the f_{H_2O} dependence of water solubility, which is indicative of the dominant dissolution mechanism of water in nominally anhydrous minerals. Almost linear dependence on f_{H_2O} of water concentration in olivine indicates that water is predominately incorporated in olivine via two hydrogen atoms substituted into a Mg-site vacancy under the condition we explored.

The proposed method can be applicable to a wider range of *P*–*T* conditions (*P* up to 50 GPa and *T* up to 1500 °C) with various f_{H_2O} buffers involving dense hydrous silicate phases in the MgO–SiO_2–H_2O system (e.g., Kawamoto, 2006) as well as the Al_2O_3–SiO_2–H_2O system (e.g., Sano et al., 2004). Since the chemical system of the f_{H_2O} buffer is separated from that of the specimen (except hydrogen activity), the range of *P*–*T* conditions which can be explored are bounded to the stability field of the individual water fugacity assemblage (and the specimen). With a minor modification of sample assemblage, the proposed method can be applicable to investigate not only water solubility but also other related properties such as water partitioning between mantle minerals, the

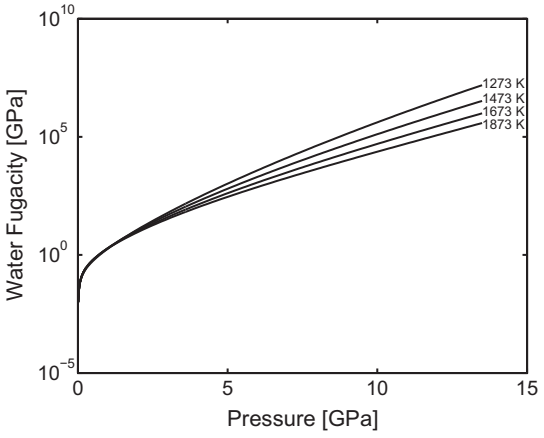

Fig. A1. Fugacity of water as a function of pressure and temperature based on the equation of state by Frost and Wood (1997).

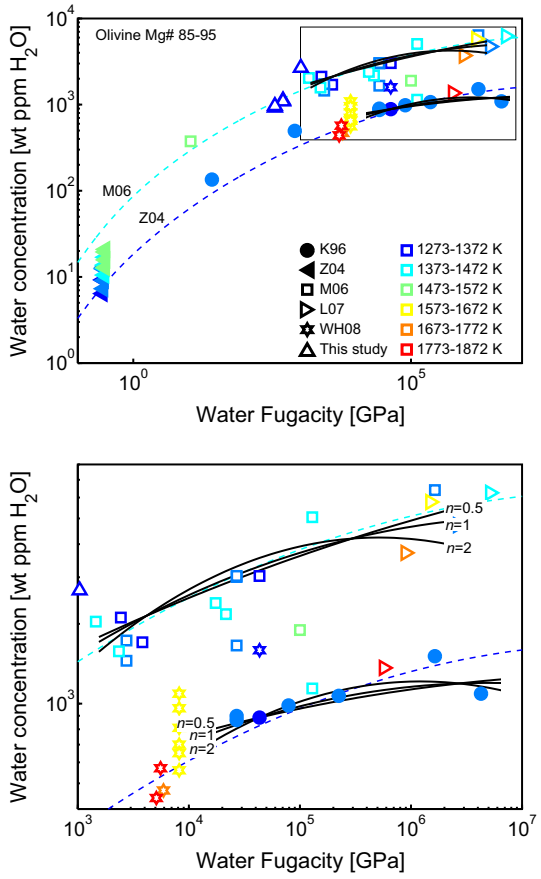

Fig. A2. Water solubility in olivine with Mg# 85–95 at pressure from 300 MPa to 14 GPa and temperature from 1273 to 1773 K plotted against water fugacity. The bottom figure is the expansion of the rectangular area of the top figure. Symbol indicates the data source; K96: Kohlstedt et al. (1996); Z04: Zhao et al. (2004); M06: Mosenfelder et al. (2006); L07: Litasov et al. (2007); WH08: Withers and Hirschmann (2008); and this study. Solid symbols are data using the calibration by Paterson (1982), and open symbols using Bell et al. (2003). Color of the symbols indicates annealing temperature. Two dashed lines were water solubility calculated from Zhao et al. (2004) for Z04 and Mosenfelder et al. (2006) for M06, respectively, and the solid lines are calculated based on the data by Kohlstedt et al. (1996) and Mosenfelder et al. (2006) at pressure higher than 5 GPa using the equation given in the text with three different fugacity exponent values: $n = 0.5$, 1 and 2.

influence of water on transport properties including rheological properties and electrical conductivity, and water concentration at the incipient of melting.

Acknowledgements

We are grateful to Takaaki Kawazoe and Zhicheng Jing for their assistance in multianvil experiments, and Zhenting Jiang for his help in infrared spectroscopy and electron microprobe analysis. This research was financially supported by National Science Foundation under Grant No. EAR-0809330. The manuscript was improved by comments from two anonymous reviewers.

Appendix A

In most of water-sensitive properties (strain-rate, hydrogen solubility, electrical conductivity and diffusion coefficient), the influence of water on a property in nominally anhydrous minerals is often described as a function of water fugacity f_{H_2O} in the form:

$$X = Af_{H_2O}^{n} \exp\left(-\frac{\Delta E^{*} + P\Delta V^{*}}{RT}\right) \quad (A1)$$

where X is the physical property of interest at temperature T and pressure P, A is a material-dependent parameter, n is the fugacity exponent, ΔE^{*} is the activation energy in case of kinetic properties or reaction enthalpies in case of water solubility, $\Delta V*$ is the activation volume in case of kinetic properties or volume change in the reaction in solid part in case of water solubility, and R is the gas constant. Among the parameters in such a relationship, the water fugacity exponent, n, and the activation volume (volume change), $\Delta V*$, are the keys to infer the microscopic mechanisms of these properties (e.g., Karato, 2008). However, determining these two parameters was difficult with previously used methods because of the following reasons. As Fig. A1 shows, water behaves like a nearly ideal gas up to P~0.3 GPa at high temperatures, and its property starts to deviate from ideal gas behavior at P~0.5 GPa such that f_{H_2O} at high pressure increases exponentially with pressure, as does the term $\exp\left(-\frac{\Delta E^{*}+P\Delta V^{*}}{RT}\right)$. Because of this similarity in the functional form with respect to pressure between f_{H_2O} and the term $\exp\left(-\frac{\Delta E^{*}+P\Delta V^{*}}{RT}\right)$ at high pressures, it is difficult to uniquely constrain two unknowns, namely n and $\Delta V*$ over a narrow pressure range of high-pressure data. In order to illustrate this tradeoff, Fig. A2 summarizes existing data for water solubility in olivine with Mg# 85–95 at pressure from 300 MPa to 14 GPa and temperature from 1273 to 1773 K (Kohlstedt et al., 1996; Litasov et al., 2007; Mosenfelder et al., 2006; Withers and Hirschmann, 2008; Zhao et al., 2004). We fitted data by Kohlstedt et al. (1996) and Mosenfelder et al. (2006) at pressure higher than 5 GPa using the Eq. A1 with three different fugacity exponent values: $n = 0.5$, 1 and 2. As shown in the Fig. A2, given the relatively large scatter of the experimental data, both data does not favor any of the three n values.

One common approach taken in the previous high-pressure studies to determine the fugacity exponent of water solubility was to fit data covering a wide range of pressure (e.g., Kohlstedt et al., 1996; Mosenfelder et al., 2006). The underlying assumption of this approach is that the water dissolution mechanism does not change with pressure and other thermochemical conditions, which was examined indirectly by observing the similarity in OH stretching modes in the infrared spectra of recovered samples. The validity of this assumption of the same defect-type for a bread pressure range is not secure because hydrogen defects in olivine are located at several different sites such as Mg-site or Si-site vacancies (e.g., Keppler and Bolfan-Casanova, 2006), and their relative abundance likely changes with thermochemical conditions including pressure, temperature and water concentration. Consequently, we conclude that previous studies are subject to uncertainties in inferring the microscopic mechanisms of water-related properties because either (1) it is difficult to separate the f_{H_2O} effect from that of the intrinsic pressure-volume term within the narrow pressure interval at high pressure or (2) it is hard to examine whether the mechanism of water-related properties changes over the wide range of pressure interval. In contrast to these approaches, we proposed a method to control f_{H_2O} as an independent variable at constant pressure and temperature. By using this method, the dissolution mechanisms of water or other water-related properties can be investigated at fixed condition of pressure and temperature.

References

Bai, Q., Kohlstedt, D.L., 1993. Effects of chemical environment on the solubility and incorporation mechanism for hydrogen in olivine. Phys. Chem. Miner. 19 (7), 460–471.

Bali, E., Bolfan-Casanova, N., Koga, K.T., 2008. Pressure and temperature dependence of H solubility in forsterite: an implication to water activity in the Earth interior. Earth Planet. Sci. Lett. 268 (3–4), 354–363. doi:10.1016/j.epsl.2008.01.035.

Bell, D.R., Rossman, G.R., Maldener, J., Endisch, D., Rauch, F., 2003. Hydroxide in olivine: a quantitative determination of the absolute amount and calibration of the IR spectrum. J. Geophys. Res. 108 (B2). doi:10.1029/2001JB000679.

Costa, F., Chakraborty, S., 2008. The effect of water on Si and O diffusion rates in olivine and implications for transport properties and processes in the upper mantle. Phys. Earth Planet. Inter. 166, 11–29. doi:10.1016/j.pepi.2007.10.006.

Edgar, A.D., 1973. Experimental Petrology: Basic Principles and Techniques. Clarendon Press, Oxford, p. 217.

Frost, D., Wood, B.J., 1997. Experimental measurements of the properties of H_2O–CO_2 mixtures at high pressures and temperatures. Geochim. Cosmochim. Acta 61 (16), 3301–3309.

Fukui, H., Inoue, T., Yasui, T., Katsura, T., Funakoshi, K., Ohtaka, O., 2005. Decomposition of brucite up to 20 GPa: evidence for high MgO-solubility in the liquid phase. Eur. J. Miner. 17, 261–267. doi:10.1127/0935-1221/2005/0017-0261.

Hier-Majumder, S., Anderson, I.M., Kohlstedt, D.L., 2005. Influence of protons on Fe–Mg interdiffusion in olivine. J. Geophys. Res. 110 (B2). doi:10.1029/2004JB003292.

Hirth, G., Kohlstedt, D., 2003. Rheology of the upper mantle and the mantle wedge: a view from the experimentalist. In: Eiler, J. (Ed.). Inside the Subduction Factory Am Geophys Union Monogr 138, 83–105.

Inoue, T., 1994. Effect of water on melting phase relations and melt composition in the system Mg_2SiO_4–$MgSiO_3$–H_2O up to 15 GPa. Phys. Earth Planet. Inter. 85, 237–263.

Johnson, M., Walker, D., 1993. Brucite [$Mg(OH)_2$] dehydration and the molar volume of H_2O to 15 GPa. Am. Miner. 78, 271–284.

Keppler, H., Bolfan-Casanova, N., 2006. Thermodynamics of water solubility and partitioning. Rev. Miner. Geochem. 62, 193–230. doi:10.2138/rmg.2006.62.9.

Karato, S., 2008. Deformation of Earth Materials: Introduction to the Rheology of the Solid Earth. Cambridge University Press, Cambridge, pp. 463.

Karato, S., Jung, H., 2003. Effects of pressure on high-temperature dislocation creep in olivine. Philos. Mag. 83 (3), 401–414.

Kawamoto, T., 2004. Hydrous phase stability and partial melt chemistry in H_2O-saturated KLB-1 peridotite up to the uppermost lower mantle conditions. Phys. Earth Planet. Inter., 387–395. doi:10.1016/j.pepi.2003.06.003.

Kawamoto, T., 2006. Hydrous phases and water transport in the subducting slab. Rev. Miner. Geochem. 62, 273–289. doi:10.2138/rmg.2006.62.12.

Kohlstedt, D.L., Keppler, H., Rubie, D.C., 1996. Solubility of water in the alpha, beta and gamma phases of $(Mg, Fe)_2SiO_4$. Contrib. Miner. Petrol. 123 (4), 345–357.

Komabayashi, T., Omori, S., 2006. Internally consistent thermodynamic data set for dense hydrous magnesium silicates up to 35 GPa, 1600 degrees C: implications for water circulation in the Earth's deep mantle. Phys. Earth Planet. Inter. 156 (1–2), 89–107. doi:10.1016/j.pepi.2006.02.002.

Komabayashi, T., Omori, S., Maruyama, S., 2005. Experimental and theoretical study of stability of dense hydrous magnesium silicates in the deep upper mantle. Phys. Earth Planet. Inter. 153 (4), 191–209. doi:10.1016/j.pepi.2005.07.001.

Litasov, K.D., Ohtani, E., Kagi, H., Jacobsen, S.D., Ghosh, S., 2007. Temperature dependence and mechanism of hydrogen incorporation in olivine at 12.5–14.0 GPa. Geophys. Res. Lett. 34 (16). doi:10.1029/2007GL030737.

Mei, S., Kohlstedt, D.L., 2000. Influence of water on plastic deformation of olivine aggregates: 1. Diffusion creep regime. J. Geophys. Res. 105 (B9), 21457–21469.

Mibe, K., Fujii, T., Yasuda, A., 2002. Composition of aqueous fluid coexisting with mantle minerals at high pressure and its bearing on the differentiation of the Earth's mantle. Geochim. Cosmochim. Acta 66 (12), 2273–2285.

Mibe, K., Kanzaki, M., Kawamoto, T., Kyoko, M.N., Fei, Y., Ono, S., 2007. Second critical endpoint in the peridotite–H_2O system. J. Geophys. Res., 112. doi:10.1029/2005JB004125.

Mosenfelder, J.L., Deligne, N.I., Asimow, P.D., Rossman, G.R., 2006. Hydrogen incorporation in olivine from 2 to 12 GPa. Am. Miner. 91 (2–3), 285–294. doi:10.2138/am.2006.1943.

Otsuka, K., McCammon, C.A., Karato, S., 2010. Tetrahedral occupancy of ferric iron in (Mg,Fe)O: implications for point defects in the Earth's lower mantle. Phys. Earth Planet. Inter. 180 (3–4), 179–188. doi:10.1016/j.pepi.2009.10.005.

Paterson, M.S., 1982. The determination of hydroxyl by infrared-absorption in quartz, silicate-glasses and similar materials. Bull. Miner. 105 (1), 20–29.

Sano, A., Ohtani, E., Kubo, T., Funakoshi, K., 2004. In situ X-ray observation of decomposition of hydrous aluminum silicate $AlSiO_3OH$ and aluminum oxide hydroxide d-AlOOH at high pressure and temperature. J. Phys. Chem. Sol. 65, 1547–1554.

Thompson, J.B., 1982. Composition space: an algebraic and geometric approach. Rev. Miner. Geochem. 10, 1–31.

Wang, D.J., Mookherjee, M., Xu, Y.S., Karato, S., 2006. The effect of water on the electrical conductivity of olivine. Nature 443 (7114), 977–980. doi:10.1038/nature05256.

Withers, A.C., Hirschmann, M.M., 2008. Influence of temperature, composition, silica activity and oxygen fugacity on the H_2O storage capacity of olivine at 8 GPa. Contrib. Miner. Petrol. 156 (5), 595–605. doi:10.1007/s00410-008-0303-3.

Yamamoto, K., Akimoto, S., 1977. The system MgO–SiO_2–H_2O at high pressures and temperatures – stability filed for hydroxyl-chondrodite, hydroxyl-clinohumite and 10 Å phase. Am. J. Sci. 277, 288–312.

Yoshino, T., Matsuzaki, T., Shatskiy, A., Katsura, T., 2009. The effect of water on the electrical conductivity of olivine aggregates and its implications for the electrical structure of the upper mantle. Earth Planet. Sci. Lett. 288 (1–2), 291–300. doi:10.1016/j.epsl.2009.09.032.

Wunder, B., 1998. Equilibrium experiments in the system MgO ± SiO_2 ± H_2O (MSH): stability fields of clinohumite-OH [$Mg_9Si_4O_{16}(OH)_2$], chondrodite-OH [$Mg_5Si_2O_8(OH)_2$] and phase A ($Mg_7Si_2O_8(OH)_6$). Contrib. Miner. Petrol. 132, 111–120.

Zhao, Y.H., Ginsberg, S.B., Kohlstedt, D.L., 2004. Solubility of hydrogen in olivine: dependence on temperature and iron content. Contrib. Miner. Petrol. 147, 155–161. doi:10.1007/s00410-003-0524-4.